European Journal of Immunology

Tissue immunology and leukocyte trafficking

Basic

Research Article

Comprehensive characterization of myeloid cells during wound healing in healthy and healing-impaired diabetic mice

Natasha Joshi, Lea Pohlmeier*, Maya Ben-Yehuda Greenwald, Eric Haertel, Paul Hiebert, Manfred Kopf and Sabine Werner*

Institute of Molecular Health Sciences, Department of Biology, ETH Zurich, Zurich, Switzerland

Wound healing involves the concerted action of various lymphoid and in particular myeloid cell populations. To characterize and quantitate different types of myeloid cells and to obtain information on their kinetics during wound healing, we performed multiparametric flow cytometry analysis. In healthy mice, neutrophil numbers increased early after injury and returned to near basal levels after completion of healing. Macrophages, monocyte-derived dendritic cells (DCs), and eosinophils were abundant throughout the healing phase, in particular in early wounds, and Langerhans cells increased after wounding and remained elevated after epithelial closure. Major differences in healing-impaired diabetic mice were a much higher percentage of immune cells in late wounds, mainly as a result of neutrophil, macrophage, and monocyte persistence; reduced numbers and percentages of macrophages and monocyte-derived DCs in early wounds; and of Langerhans cells, conventional DCs, and eosinophils throughout the healing process. Finally, unbiased cluster analysis (PhenoGraph) identified a large number of different clusters of myeloid cells in skin wounds. These results provide insight into myeloid cell diversity and dynamics during wound repair and highlight the abnormal inflammatory response associated with impaired healing.

Keywords: Inflammation · Myeloid cell · Skin · Tissue repair · Wound healing

Additional supporting information may be found online in the Supporting Information section at the end of the article.

Introduction

Wound healing is a complex process involving various skin-resident and invading immune cells [1–4]. Three overlapping phases, including inflammation, proliferation, and tissue remodeling, characterize the normal healing process [1]. Wound repair is delayed in diabetic patients and also in diabetic mice, making the latter a valuable model system to study impaired healing and the effect of various therapeutic regimens [5, 6]. The diabetes-associated healing impairment is at least in part a consequence of enhanced wound inflammation with alterations in the number and activity of myeloid cells, although the contributions of the individual immune cell types to the healing abnormalities remain to be determined [7–10].

Langerhans cells (LCs) and a subset of dermal macrophages are already present prenatally in the skin [11]. Most other myeloid cells, however, are recruited to the wound during the course of healing [12–16], and a subset of dermal macrophages as well as

Correspondence: Prof. Sabine Werner and Prof. Manfred Kopf
e-mail: sabine.werner@biol.ethz.ch; manfred.kopf@biol.ethz.ch

*Both authors contributed equally to this work.

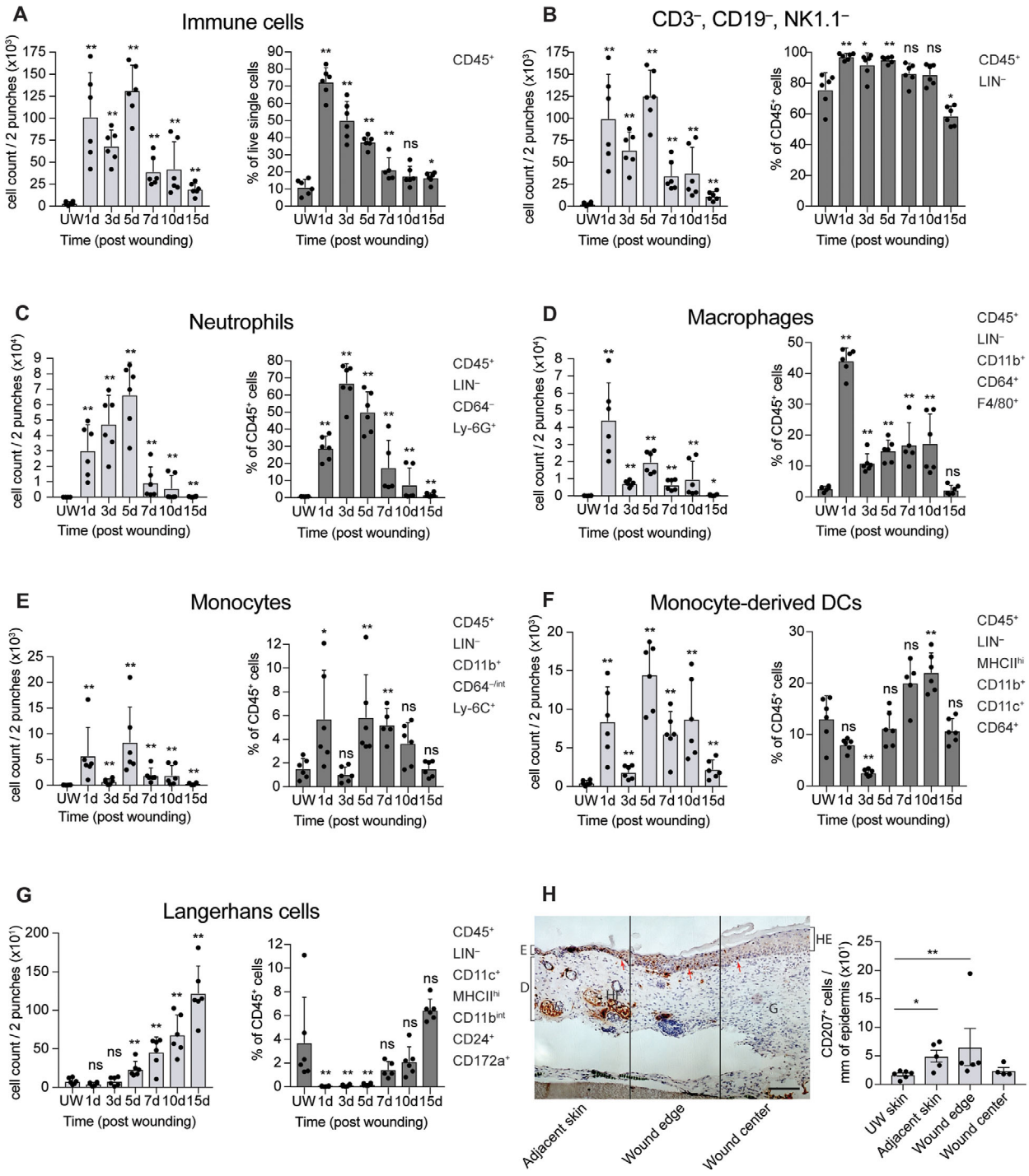

monocytes arise from hematopoietic stem cells [11]. Neutrophils are the first immune cells to arrive at the wound site due to their abundance in the circulation. They participate in the defense against invading pathogens by releasing antimicrobial peptides, proteases, reactive oxygen species (ROS), and neutrophil extracellular traps [17, 18]. In addition, they secrete proteins that attract monocytes/macrophages and activate various resident cells [19]. If the wound is not infected, neutrophils undergo apoptosis and are engulfed by macrophages. In the absence of infection, neutrophil depletion did not affect wound repair in guinea pigs [20]. Under certain conditions these cells even have a negative effect on wound healing [21], and excessive formation of neutrophil extracellular traps contributes to the impaired healing of diabetic mice and humans [22, 23].

Interestingly, mice lacking all myeloid cells showed scarless healing of small skin wounds [24], suggesting that also macrophages are dispensable for wound healing, at least under sterile conditions. However, macrophage depletion severely affected healing of larger excisional wounds in guinea pigs [25]. Deletion of the C-C chemokine receptor type 2 strongly reduced the number of monocytes in excisional mouse wounds. This attenuated wound angiogenesis and myofibroblast differentiation, while wound closure was not affected [26]. Depletion of monocytes/macrophages at different stages of wound healing further revealed their important roles in re-epithelialization and granulation tissue formation [27–29].

There is little information on the role of LCs in wound repair, but early repopulation of the epidermis by these cells after wounding and an increased LC number at the wound site correlated with better healing of diabetic ulcers in humans [30].

Plasmacytoid DCs infiltrate the wound early after injury and produce type I interferons that contribute to early immune responses and rapid wound re-epithelialization [31]. By contrast, there is as yet little information on the presence and function of conventional DCs (cDCs) in healing wounds.

To further elucidate the function of different types of myeloid cells in wound healing, it is important to determine their dynamics during the healing process. So far, most studies focused on only one or two time points and/or on a specific myeloid cell population in either healthy or diabetic mice. Therefore, we comprehensively analyzed the various myeloid cell subpopulations prior to injury and during the course of healing in both types of mice. The results obtained in this study provide the basis for a future functional characterization of these cell types and their potential use as targets for the treatment of impaired healing.

Results

Dynamic increase in myeloid cells during wound healing in C57BL/6 mice

To investigate the kinetics of myeloid cells during wound healing, we performed flow cytometry analysis of unwounded skin and of wounds at different stages of healing and early scar formation. We chose day 1, 3, 5, 7, 10, and 15 after wounding, since these time points represent characteristic phases of the healing process, including the early inflammatory phase (days 1 and 3), the phase of re-epithelialization and granulation tissue formation (days 5 and 7), and the phase of tissue remodeling (days 10 and 15). Re-epithelialization in this mouse model is usually completed at around day 7 [1, 32].

We optimized a skin/wound tissue dissociation protocol and used a flow cytometry procedure with a panel of 16 antibodies (14 colors) and a gating strategy that is suitable to identify the vast majority of myeloid cell populations in the skin [11, 33–36] (Supporting Information Fig. 1A–C). We gated on singlet, live $CD45^+$ cells and excluded lineage-positive cells (i.e., natural killer (NK) cells, B cells, and T cells) to characterize neutrophils, macrophages, monocytes, LCs, monocyte-derived DCs, and cDC subsets 1 and 2 (cDC1 and cDC2). Innate lymphocytes were not gated out in the lineage gate and not further defined in the $CD45^+$ cell gate. Mast cells were also not included, since they are scarce in the wound tissue and their kinetics has been described [4, 37, 38].

Figure 1. Kinetics of total immune and myeloid cells and their subpopulations during wound healing in C57BL/6 mice. (A–G and I, J) Flow cytometry analysis of unwounded skin (UW) and of 1-, 3-, 5-, 7-, 10-, and 15-day wounds from C57BL/6 mice using the gating strategy shown in Supporting Information Fig. 1. Wounds were generated on different days and all mice were sacrificed on the same day to allow a direct comparison. Tissue samples were analyzed by flow cytometry immediately after sacrifice. Absolute numbers are shown in the left panels and percentages are shown in the right panels. Markers used for the analysis of each cell type are shown on the right-hand side of each graph. (A) Total number of immune cells ($CD45^+$) and percentage among all live cells. (B) Total number of nonlymphoid cells ($CD45^+LIN^-$) and percentage among all $CD45^+$ cells. (C) Total number of neutrophils ($CD45^+LIN^-CD64^-Ly6G^+$) and percentage among all $CD45^+$ cells. (D) Total number of macrophages ($CD45^+LIN^-CD11b^+CD64^+F4/80^+$) and percentage among all $CD45^+$ cells. (E) Total number of monocytes ($CD45^+LIN^-CD11b^+CD64^{-/int}Ly6C^+$) and percentage among all $CD45^+$ cells. (F) Total number of monocyte-derived DCs ($CD45^+LIN^-MHCII^{hi}CD11b^+CD11c^+CD64^+$) and percentage among all $CD45^+$ cells. (G) Total number of LCs ($CD45^+LINCD11c^+MHCII^{hi}CD11b^{int}CD24^+CD172a^+$) and percentage among all $CD45^+$ cells. (H) Representative CD207 (langerin) immunohistochemistry staining of a 10-day wound section and counterstaining with hematoxylin. Scale bar: 100 μm. D: dermis, E: epidermis, G: granulation tissue, HE: hyperthickened wound epidermis, HF: hair follicle (left panel). Quantification of $CD207^+$ cells per mm of wound/skin length (right panel). (I) Total number of cDC1 ($CD45^+LIN^-CD11c^+MHCII^{hi}CD11b^{int}CD24^+CD172a^-XCR1^+$) and percentage among all $CD45^+$ cells. (J) Total number of cDC2 ($CD45^+LIN^-CD11c^+MHCII^{hi}CD11b^+CD64^-CD172a^+$) and percentage among $CD45^+$ cells. Bars indicate mean ± SD. Each time point was compared to unwounded skin using pairwise comparison, Mann–Whitney *U* rank test. $^*p \le 0.05$; $^{**}p \le 0.01$. n.s.: nonsignificant. (A–G and I and J) Each data point represents a pool of two wounds per mouse. $N = 5$ mice and $n = 5$ wound samples (pools of two wounds) for 10-day wounds; $N = 6$, $n = 6$ for all other time points. The results for unwounded skin and 1-, 5-, 10-, and 15-day wounds were verified in a second, independent experiment (see Fig. 6) and the results for unwounded skin and 3- and 5-day wounds were verified in a third experiment ($N = 4$, $n = 4$; data not shown). H: Each data point represents a section from an individual mouse. $N = 6$ for UW, $N = 5$ for adjacent skin and wound edge, $N = 4$ for wound center. Data from one experiment; the distribution of LCs in 10-day wounds was reproduced in a second experiment. Scale bar: 100 μm; magnification 20×.

Myeloid cells outnumbered lymphocytes in unwounded skin. Among all non-B, non-T, and non-NK cells ($CD45^+LIN^-$), cDC2s were most abundant, followed by monocyte-derived DCs and LCs. Other myeloid cell types were present at only low numbers and frequencies (Supporting Information Fig. 2A).

Immune cell numbers ($CD45^+$) increased strongly between days 1 and 5 after wounding compared to unwounded skin (Fig. 1A). Their absolute numbers reached a peak at day 5, with nonlymphoid cells ($CD45^+LIN^-$) comprising more than 95% of all immune cells (Fig. 1A and B). Total immune cell and nonlymphoid cell numbers subsequently declined, but they were still more abundant compared to unwounded skin at day 15 post injury (Fig. 1A), when an early scar tissue had formed (see, for example, Ref. [39]).

As expected, neutrophils ($CD45^+LIN^-CD64^-Ly6G^+$) were recruited to the wounds early after injury and their numbers and percentages peaked between days 3 and 5, followed by a gradual decline. They were by far the most abundant immune cells during the first five days of healing (Fig. 1C). Macrophage ($CD45^+LIN^-CD11b^+CD64^+F4/80^+$) numbers and percentages peaked 1 day after wounding. There was a second peak at around day 5, followed by a decline to almost basal levels (Fig. 1D). Absolute numbers and percentages of monocytes ($CD45^+LIN^-CD11b^+CD64^{-/int}Ly6C^+$) and monocyte-derived DCs ($CD45^+LIN^-MHCII^{hi}CD11b^+CD11c^+CD64^+$) were elevated at day 1 after wounding and reached a second peak during the phase of new tissue formation (days 5–10; Fig. 1E and F).

Major histocompatibility complex II (MHCII) is mainly expressed by APCs and is required to present exogenous antigens to $CD4^+$ T cells [40]. Due to the previously demonstrated importance of MHCII for wound repair in mice [41], we analyzed the numbers and percentages of $MHCII^+$ LCs and DCs. Remarkably, LCs ($CD45^+LIN^-CD11c^+MHCII^{hi}CD11b^{int}CD24^+CD172a^+$) increased continuously after wounding until the late stages (Fig. 1G). We verified this result by immunohistochemistry staining of 10-day wounds and found a strong accumulation of CD207 (langerin)-positive cells at the wound edge (Fig. 1H). The numbers and percentages of cDC1s ($CD45^+LIN^-CD11c^+MHCII^{hi}CD11b^{int}CD24^+CD172a^-XCR1^+$) decreased early after wounding, probably due to their migration to the lymph nodes. However, as the wounds healed, their numbers increased and were higher than in normal skin after day 7 (Fig. 1I). Numbers of cDC2s ($CD45^+LIN^-CD11c^+MHCII^{hi}CD11b^+CD64^-CD172a^+$) peaked around day 5 after wounding and were generally higher than cDC1 numbers (Fig. 1J).

Identification of myeloid cell clusters in wounds using unbiased, multiparametric data analysis

Traditional gating strategies rely on prior knowledge and know-how of the researcher, thus potentially losing novel information [42, 43]. To address this concern, we used an unbiased approach to analyze the flow cytometry data. Application of the dimensionality reduction algorithm "t-Distributed Stochastic Neighbor Embedding" (t-SNE) as well as the clustering algorithm PhenoGraph identified 25 clusters (Fig. 2A and B). A representation of manually gated cell populations on t-SNE maps shows that manual gating covered almost all clusters found by PhenoGraph clustering (Fig. 2C), except clusters 14 and 23, which are live, $CD45^+CD11b^+CD24^+$. Their further analysis in normal skin revealed that they are positive for Siglec-F^+, indicating that they depict eosinophils (Supporting Information Fig. 2B). While LCs and cDC1s formed their own clusters (11 and 1, respectively), PhenoGraph identified subpopulations among the manually gated populations. Monocytes and cDC2s were predominantly made up of two populations—clusters 4 and 5 and clusters 2 and 3, respectively. Monocyte-derived DCs were found in clusters 12, 15, 17, 22, 24, and 25. Neutrophils were split among clusters 7–10, 20, and 21, while macrophages were split among clusters 6, 13, 14, 16, 18, and 19. To understand the subclustering of certain populations, we depicted all markers monitored through color mapping of the t-SNE plots (Fig. 2D) as well as the distinct expression patterns of all markers in each cluster (Fig. 2E). This revealed that marker intensity diverted in the mean fluorescence intensity (MFI) in one cluster compared to another cluster of the same cell population. These changes in MFI can occur due to differential expression of a certain marker or variation in autofluorescence. To understand how close clusters are related to each other, we ran a hierarchical cluster analysis depicted as a dendrogram, which, for example, showed the strong relationship between monocytes and macrophages (Fig. 2E, right side).

When splitting the t-SNE map by time points (Supporting Information Fig. 3A), we observed changes in the composition of clusters for each cell type. Some clusters were predominantly seen in unwounded skin, while others only appeared after wounding (Supporting Information Fig. 3A). The composition of neutrophils, macrophages, and monocyte-derived DCs underwent changes during the observed time period with the proportion of certain subclusters rising and falling, while the monocyte composition was relatively stable (Supporting Information Fig. 3B–E).

Kinetics of myeloid cells during wound healing in C57BLKSJ-lepr$^{db/db}$ mice

In a separate experiment, we used the same gating strategy to analyze myeloid cell kinetics in healing-impaired genetically diabetic C57BLKSJ-lepr$^{db/db}$ mice, which develop type II diabetes due to a mutation in the leptin receptor [5]. These mice only showed complete re-epithelialization at around day 8 after wounding, while granulation tissue formation was even further delayed (Ben-Yehuda Greenwald et al., unpubl. data).

In contrast to unwounded skin of healthy mice (Supporting Information Fig. 2A), there was a slight excess of lymphocytes compared to myeloid cells in unwounded skin of diabetic mice (Supporting Information Fig. 4, top panel). Among the latter, the distribution was similar as in healthy mice with the exception of a reduced frequency of cDC2s and a higher abundance of

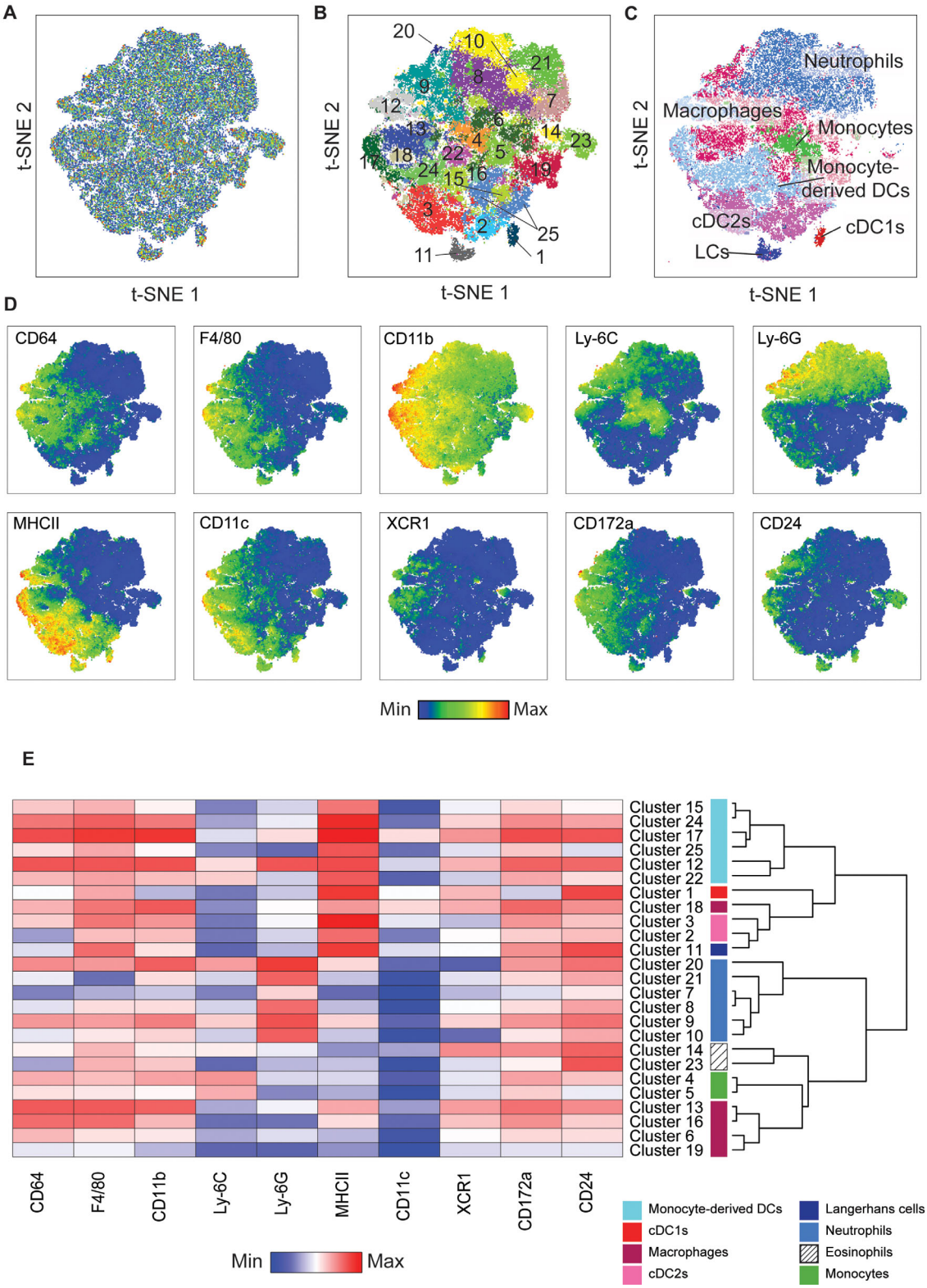

Figure 2. Unbiased, multiparametric analysis of myeloid cell kinetics during wound healing in C57BL/6 mice. Results obtained in the experiment shown in Fig. 1 were used for the analysis and all data points were included. To perform t-SNE and PhenoGraph, data from unwounded and wounded skin of all time points and all mice were pooled; the information about the origin of each cell was retained. (A) t-SNE dimensionality reduction map of pooled cytometry data from unwounded and wounded skin. (B) The 25 clusters found by PhenoGraph analysis, depicted on t-SNE map. (C) Manually gated cell populations displayed on t-SNE map. (D) Color mapping showing the intensity of staining (sinh transformed) of the indicated proteins. (E) Heatmap showing the level of expression of the various markers within each cluster (left) and dendrogram showing the relative relationship between clusters (right).

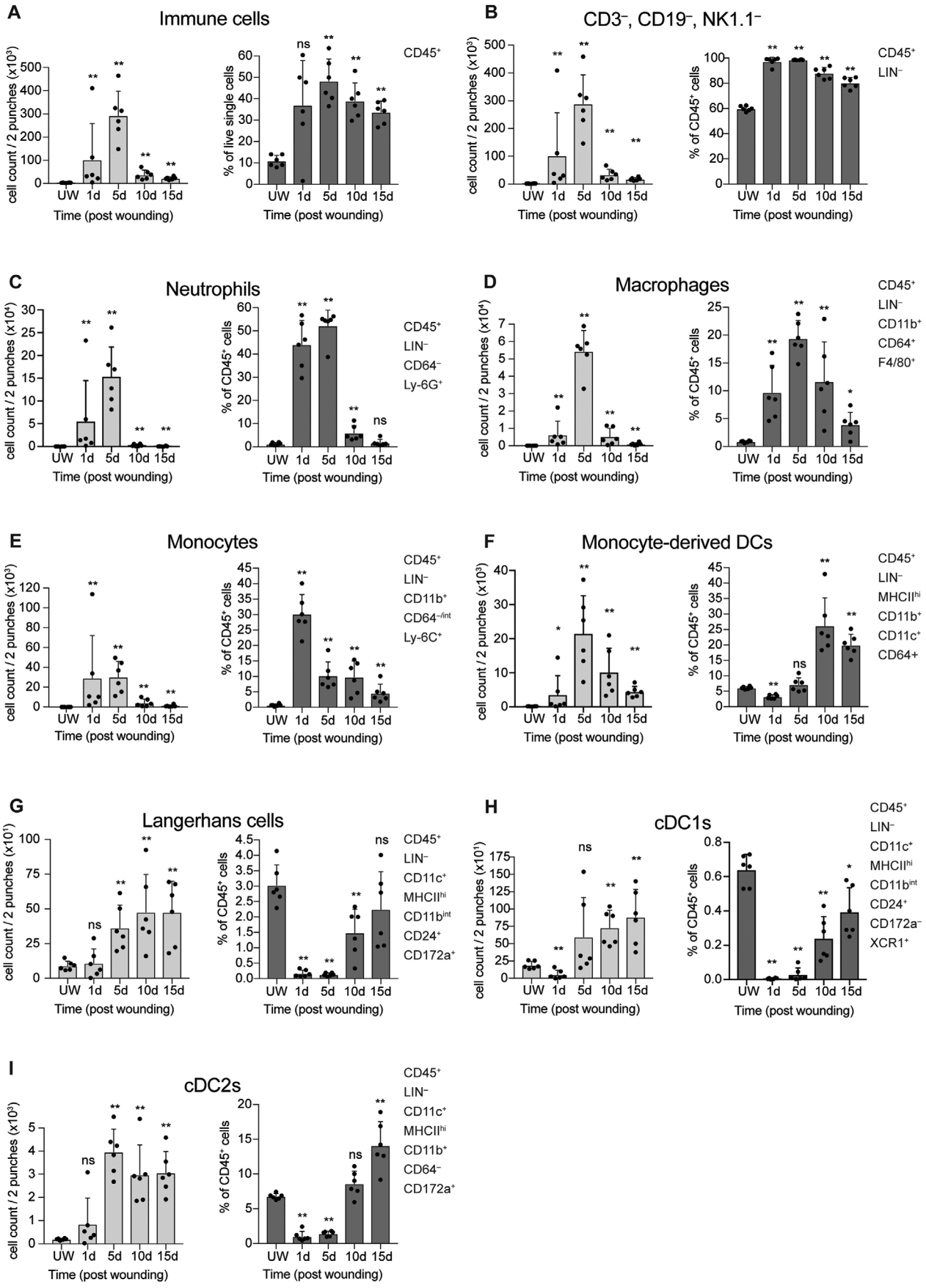

neutrophils and LCs in diabetic animals (Supporting Information Figs. 2A and 4, lower panel).

Upon wounding, total immune cells peaked a bit later than in healthy mice, but they still represented more than 30% of the live cells up to day 15 (Fig. 3A and B). Among them, the vast majority were nonlymphoid cells until day 5 (Fig. 3B).

Neutrophils were particularly abundant between days 1 and 5, and they represented more than 50% of all immune cells at day 5 (Fig. 3C). Macrophage numbers were still low at day 1 after wounding, but peaked at day 5 and subsequently declined (Fig. 3D). Monocyte numbers peaked between days 1 and 5 and frequencies peaked at day 1, followed by a continuous decline (Fig. 3E). Counts of monocyte-derived DCs peaked at day 5 and remained elevated at day 15 (Fig. 3F). LCs and cDC1s increased gradually as healing progressed and remained elevated compared to uninjured skin at the late time points (Fig. 3G and H). cDC2s were most abundant between days 5 and 10 postwounding (Fig. 3I). The percentage of LCs, cDC1s, and cDC2s dropped after wounding and then increased again concomitantly with the reduction in neutrophils and macrophages (Fig. 3G–I).

Identification of myeloid cell clusters in diabetic wounds using multiparametric data analysis

Unbiased analysis of the data from the diabetic mice revealed 20 clusters (Fig. 4A and B), and PhenoGraph identified subpopulations among the manually gated populations that express different levels of various immune cell marker proteins (Fig. 4C–E). Clusters 1, 4, and 5 represent neutrophils, while macrophages are split between clusters 10, 11, and 17. The most diverse population are monocyte-derived DCs, which are distributed into clusters 6, 9, 12, 15, and 19. Monocytes (clusters 3 and 8), cDC1s (cluster 2), and LCs (cluster 7) only occupy one or two clusters each. cDC2s are predominantly found in clusters 13 and 14. Cluster 18 is split between monocyte-derived DCs and cDC2s. Again, certain clusters were not covered by manual gating, in particular clusters 16 and 20. Cells from cluster 16 border the CD11b gate and are negative for all markers, indicating a minor contamination by lymphocytes. Cluster 20 was identified as eosinophils by further analysis (Supporting Information Fig. 2B).

Subclustering of certain populations as visualized through color mapping of the t-SNE plots indicates that neutrophils and other myeloid cells infiltrating the skin during wound healing also undergo phenotypical changes in db/db mice (Supporting Information Fig. 5A). The relative contribution of individual cell clusters changed over time, in particular within the macrophage, monocyte, and monocyte-derived DC clusters (Supporting Information Fig. 5B–E).

Modeling the kinetics of myeloid cell presence in wounds of healthy and diabetic mice

To further identify the most likely kinetics of myeloid cell presence in the skin after wounding based on the analysis of individual time points, we used the nonparametric Loess (robust locally weighted regression) technique [44, 45], which uses locally weighted least squares to fit a line to a scatter plot without the rigidity of traditional linear regression. The plot highlights that neutrophils are by far the most abundant type of myeloid cells in early wounds of healthy and diabetic mice. By contrast, monocyte-derived DCs predominated during the later phase of healing (Supporting Information Fig. 6A–D). The plots further demonstrate the continuous presence of macrophages throughout the course of healing and the presence of several less abundant myeloid cell populations. They also point to various differences in myeloid cell numbers and frequencies between healthy and diabetic mice (Supporting Information Fig. 6A–D).

Comparative analysis of myeloid cells in C57BL/6 and C57BLKSJ-lepr$^{db/db}$ mice

To directly compare the myeloid cell numbers and frequencies in healthy and diabetic mice, we analyzed normal skin and wounds (days 1, 5, 10, and 15) from additional healthy and diabetic mice in an independent experiment performed on the same day.

The total cell number as well as the number of myeloid cells was almost three times higher in C57BL/6 mice compared to diabetic mice in unwounded skin (Fig. 5A and B). This pattern reversed during the wound healing process, and on day 5 after wounding

Figure 3. Kinetics of total immune and myeloid cells and their subpopulations during wound healing in diabetic C57BLKSJ-lepr $^{db/db}$ mice. (A–I) Flow cytometry analysis of unwounded skin and of 1-, 5-, 10- and 15-day wounds from C57BLKSJ-lepr $^{db/db}$ mice using the gating strategy shown in Supporting Information Fig. 1. Wounds were generated on different days and all mice were sacrificed on the same day to allow a direct comparison. Tissue samples were analyzed by flow cytometry immediately after sacrifice. Absolute numbers are shown in the left panels and percentages are shown in the right panels. Markers used for the analysis of each cell type are shown on the right-hand side of each graph. (A) Total number of immune cells ($CD45^+$) and percentage among all live cells. (B) Total number of nonlymphoid cells ($CD45^+LIN^-$) and percentage among all $CD45^+$ cells. (C) Total number of neutrophils ($CD45^+LIN^-CD64^-Ly6G^+$) and percentage among all $CD45^+$ cells. (D) Total number of macrophages ($CD45^+LIN^-CD11b^+CD64^+F4/80^+$) and percentage among all $CD45^+$ cells. (E) Total number of monocytes ($CD45^+LIN^-CD11b^+CD64^{-/int}Ly6C^+$) and percentage among all $CD45^+$ cells. (F) Total number of monocyte-derived DCs ($CD45^+LIN^-MHCII^{hi}CD11b^+CD11c^+CD64^+$) and percentage among all $CD45^+$ cells. (G) Total number of LCs ($CD45^+LIN^-CD11c^+MHCII^{hi}CD11b^{int}CD24^+CD172a^+$) and percentage among all $CD45^+$ cells. (H) Total number of cDC1 ($CD45^+LIN^-CD11c^+MHCII^{hi}CD11b^{int}CD24^+CD172a^-XCR1^+$) and percentage among all $CD45^+$ cells. (I) Total number of cDC2 ($CD45^+LIN^-CD11c^+MHCII^{hi}CD11b^+CD64^-CD172a^+$) and percentage among all $CD45^+$ cells. Bars indicate mean ± SD. Each data point represents a pool of two wounds per mouse. $N = 6$ mice, $n = 6$ wound samples (pools of two wounds) for all time points. The results for all time points were verified in a second, independent experiment (see Fig. 6) and the results for unwounded skin and 5d wounds were verified in a third experiment ($N = 4$, $n = 4$; data not shown). Each time point was compared to unwounded skin using pairwise comparison, Mann–Whitney U rank test. $^*p \leq 0.05$; $^{**}p \leq 0.01$. ns: nonsignificant.

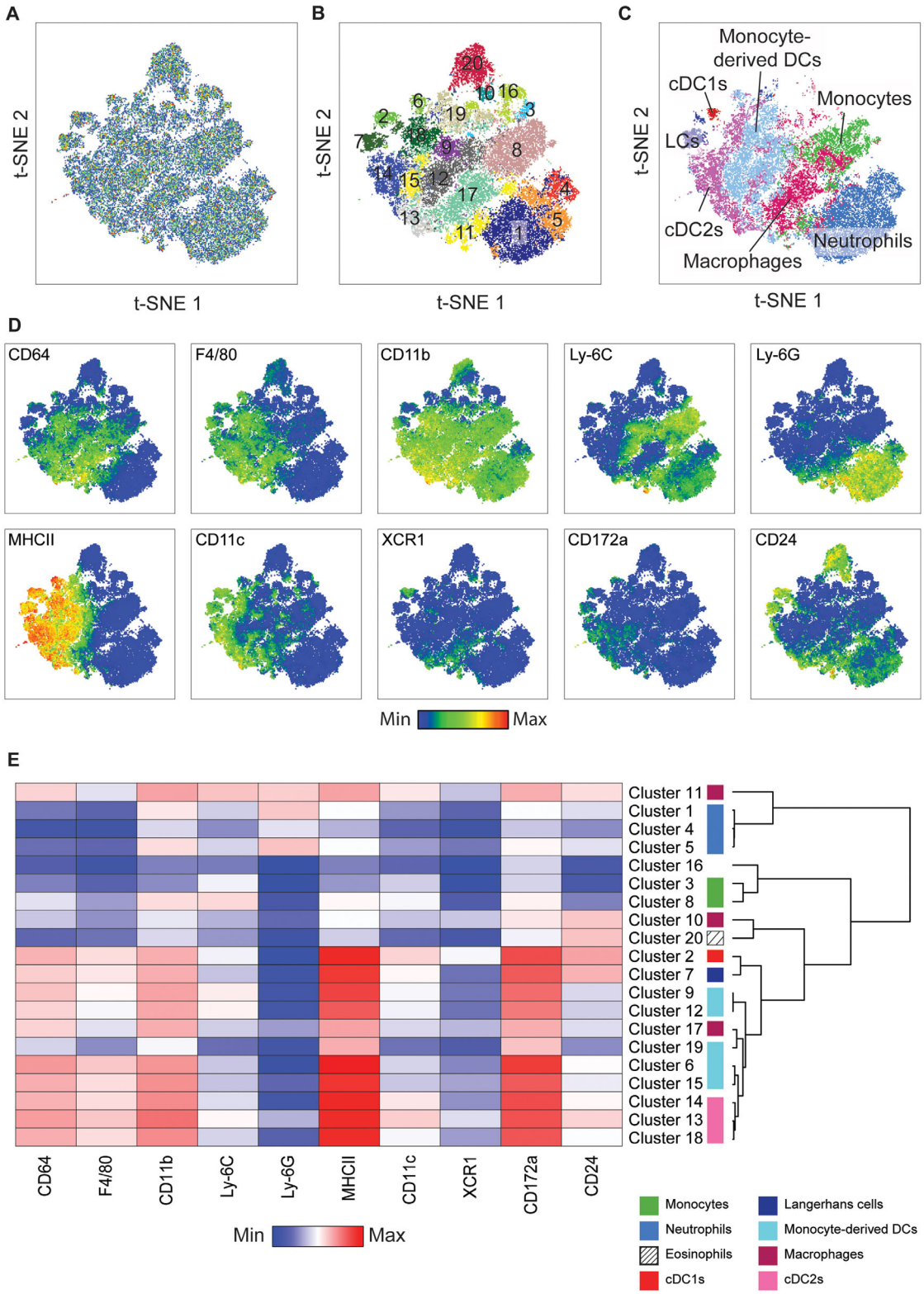

Figure 4. Unbiased, multiparametric analysis of myeloid cell kinetics during wound healing in C57BLKSJ-lepr $^{db/db}$ mice. Results obtained in the experiment shown in Fig. 3 were used for the analysis and all data points were included. To perform t-SNE and PhenoGraph, data from unwounded and wounded skin of all time points and all mice were pooled; the information about the origin of each cell was retained. (A) t-SNE map of pooled cytometry data of unwounded and wounded skin of diabetic mice. (B) The 20 clusters found by PhenoGraph analysis, depicted on a t-SNE map. (C) Manually gated cell populations displayed on t-SNE map. (D) Color mapping showing the intensity of staining (sinh transformed) of the indicated proteins. (E) Heatmap showing the level of expression of the various markers within each cluster (left) and dendrogram showing the relative relationship between clusters (right).

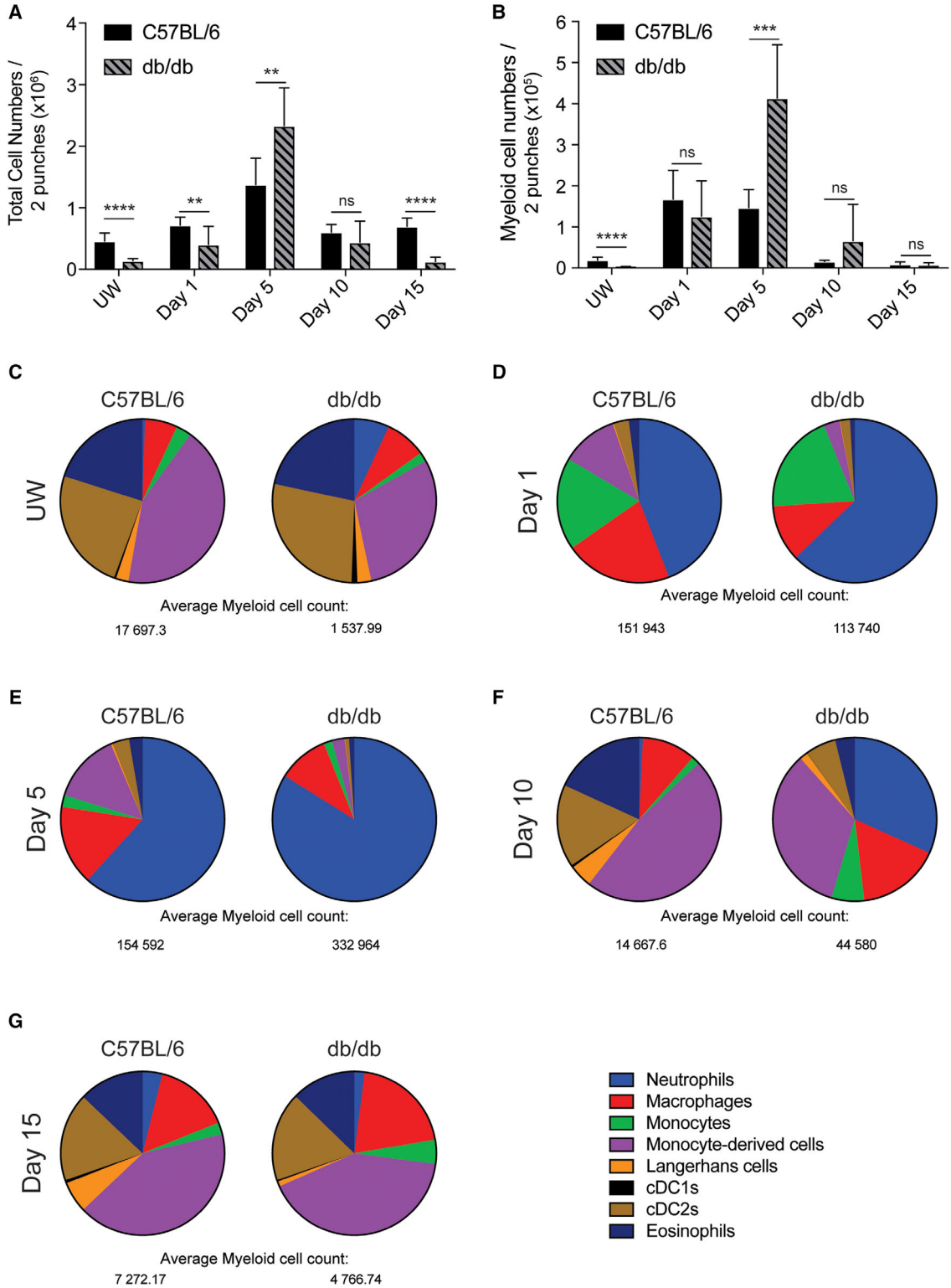

Figure 5. Myeloid cell number and composition in unwounded and wounded skin of C57BL/6 and C57BLKSJ-lepr $^{db/db}$ mice. (A) Total cell number and (B) number of myeloid cells in unwounded skin and during wound healing. Bars indicate mean ± SD. Mann–Whitney *U* rank test. $^{*}p \leq 0.05$; $^{**}p \leq 0.01$, $^{***}p \leq 0.001$, n.s.: nonsignificant. Data are from a representative experiment performed twice (see Fig. 6). (C–G) Pie charts showing the percentage of each myeloid cell population among all myeloid cells in (C) unwounded skin, and (D) 1-day, (E) 5-day, (F) 10-day, and (G) 15-day wounds of C57BL/6 (left charts) and C57BLKSJ-lepr $^{db/db}$ mice (right charts). Pie charts are based on the data shown in Fig. 6. Information about the average myeloid (nonlymphoid) cell count is provided below the charts. (A–G) $N = 4$–5 mice, $n = 8$–10 wound samples (pools of two wounds each) for C57BL/6 mice and $N = 5$, $n = 10$ for C57BLKSJ-lepr $^{db/db}$ mice. Results were reproduced in an independent experiment (see data from Figs. 1 and 3) and for NS and the 5d time point in a third experiment ($N = 4$, $n = 4$ mice; data not shown).

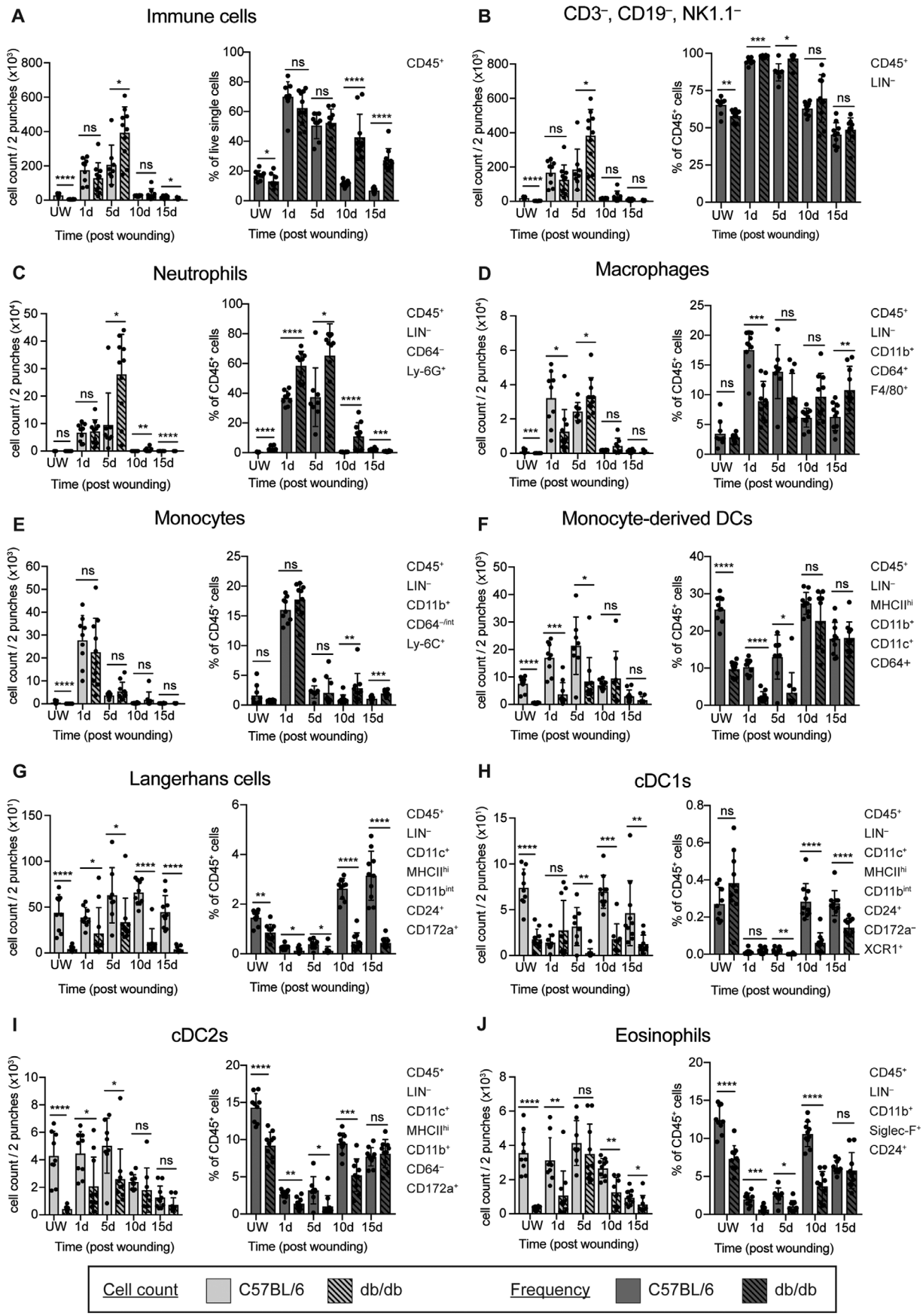

Figure 6. Direct comparison of myeloid cell numbers and frequencies in unwounded skin and wounds of C57BL/6 and C57BLKSJ-lepr $^{db/db}$ mice. (A–I) Comparative flow cytometric analysis of unwounded skin, and 1-, 5-, 10-, and 15-day wounds from nondiabetic C57BL/6 mice and diabetic C57BLKSJ-lepr$^{db/db}$ mice using the gating strategy shown in Supporting Information Fig. 1. Wounds were generated on different days and all mice were sacrificed on the same day to allow a direct comparison. Tissue samples were analyzed by flow cytometry immediately after sacrifice. Absolute numbers are shown in the left panels and percentages are shown in the right panels. Markers used for the analysis of each cell type are shown on the right-hand side of each graph. (A) Total number of immune cells ($CD45^+$) and percentage among all live cells. (B) Total number of nonlymphoid cells ($CD45^+LIN^-$) and percentage among all $CD45^+$ cells. (C) Total number of neutrophils ($CD45^+LIN^-CD64^-Ly6G^+$) and percentage among all $CD45^+$ cells. (D) Total number of macrophages ($CD45^+LIN^-CD11b^+CD64^+F4/80^+$) and percentage among $CD45^+$ cells. (E) Total number of monocytes ($CD45^+LIN^-CD11b^+CD64^{-/int}Ly6C^+$) and percentage among all $CD45^+$ cells. (F) Total number of monocyte-derived DCs ($CD45^+LIN^-MHCII^{hi}CD11b^+CD11c^+CD64^+$) and percentage among all $CD45^+$ cells. (G) Total number of LCs ($CD45^+LIN^-CD11c^+MHCII^{hi}CD11b^{int}CD24^+CD172a^+$) and percentage among all $CD45^+$ cells. (H) Total number of cDC1 ($CD45^+LIN^-CD11c^+MHCII^{hi}CD11b^{int}CD24^+CD172a^-XCR1^+$) and percentage among all $CD45^+$ cells. (I) Total number of cDC2 ($CD45^+LIN^-CD11c^+MHCII^{hi}CD11b^+CD64^-CD172a^+$) and percentage among all $CD45^+$ cells. (J) Total number of eosinophils ($CD45^+LIN^-CD11b^+Siglec\text{-}F^+CD24^+$) and percentage among all $CD45^+$ cells. Bars indicate mean ± SD. Each data point represents a pool of two wounds. C57BL/6 mice: $N = 4$ mice, $n = 8$ wound samples (pools of two wounds) for UW and 1-day wounds, $N = 4$, $n = 8$ for 5-day wounds and $N = 5$, $n = 10$ for all other time points); C57BLKSJ-lepr $^{db/db}$ mice: $N = 5$, $n = 10$ for all time points. Numbers and frequencies in healthy versus diabetic mice were compared for each time point. Mann–Whitney U rank test. $^{*}p \le 0.05$, $^{**}p \le 0.01$, $^{***}p \le 0.001$, $^{****}p \le 0.0001$; n.s.: nonsignificant. Results were verified in independent experiments with healthy and diabetic mice analyzed at different days (see Figs. 1 and 3). Results for unwounded skin and 5-day wounds were verified in a third experiment with healthy and diabetic mice analyzed on the same day ($N = 4$; $n = 4$; data not shown).

the total cell number and the number of myeloid cells was significantly higher in diabetic mice. On day 15, the total cell number returned to the ratio seen in unwounded skin, while the number of myeloid cells was comparable in both types of mice at this stage.

The contributions of different types of nonlymphoid cells to the complete immune cell pool in unwounded skin and at different time points after injury of healthy and diabetic mice are schematically shown as pie charts, highlighting similarities and differences between myeloid cells in both types of mice (Fig. 5C–G). The most obvious differences were seen in unwounded skin and at day 1 after wounding, indicating that immune cell alterations that are already present in unwounded skin as well as differences in the early inflammatory response contribute to the impaired healing of db/db mice.

A direct comparison of the kinetics of myeloid cells during wound healing demonstrated a much higher percentage of immune cells among all cells in diabetic wounds between days 10 and 15, reflecting the delayed healing and the impaired resolution of inflammation (Fig. 6A)

While there were no major differences in total nonlymphoid cells (Fig. 6B), neutrophils were more abundant throughout the healing process in diabetic mice (Fig. 6C). Macrophages were less abundant in early wounds of diabetic mice, but exceeded the numbers and frequencies seen in healthy mice at later stages of the repair process (Fig. 6D). No major differences were observed in the numbers and frequencies of monocytes. Monocyte-derived DCs, LCs, cDC1, and cDC2 were significantly less abundant in diabetic versus healthy mice, both in unwounded skin and in wounds at different stages (Fig. 6F–I). Finally, eosinophil numbers did not change by wounding in healthy mice, indicating that they infiltrate the clot. However, they declined after completion of healing (Fig. 6J). There was a continuous increase in the number of these cells in diabetic mice up to day 5 postwounding, followed by a decline. Importantly, however, numbers and frequencies of eosinophils were significantly lower in unwounded skin and in early and late wounds of diabetic versus healthy mice (Fig. 6J). These results suggest that enhanced numbers of neutrophils combined with reduced numbers of macrophages, monocyte-derived DCs, LCs, cDCs, and eosinophils and the resulting imbalance in the immune cell composition in wounds of diabetic mice may contribute to their impaired healing.

Discussion

A well-regulated influx and/or activation of myeloid cells early after wounding and their efflux or apoptosis at a later stage is important for proper healing and limitation of scar formation [2, 13, 46]. Surprisingly, however, quantitative data showing the kinetics of different types of myeloid cells during the course of normal and impaired wound healing are scarce. Furthermore, the available data are mainly based on immunohistochemistry/ immunofluorescence analyses. While this provides important information on the localization of different immune cells, it is difficult to obtain quantitative data of the complete wound tissue, and the number of markers that can be used for co-staining is limited.

To overcome these limitations, we optimized a protocol for immune cell isolation from murine skin [32], and combined it with a modified protocol for multicolor flow cytometry analysis of myeloid cells [11, 33–36]. The comprehensive data obtained in this study confirm previously published data, such as the early arrival of neutrophils [15], but also identify the kinetics of additional myeloid cell types and their dysregulation in uninjured and wounded skin of diabetic mice. In particular, the unbiased, multiparametric analysis of the data set allowed the identification of a multitude of myeloid cell subpopulations, of which some may represent transition stages. Their functional analysis will provide important insight into the changes in myeloid cell activity during the normal repair process and identify myeloid cell features associated with impaired healing. The latter may even serve as biomarkers for prediction of healing versus failure to heal.

The early arrival of neutrophils at the wound site is in line with the role of these cells in the defense against invading pathogens, clearing of cellular debris, and release of chemokines and cytokines to attract other effector immune cells [15, 19, 47]. Their numbers and frequencies were significantly higher in wounds of diabetic mice, suggesting that ROS and proteases produced by these cells contribute to the tissue damage and the prolongation of the repair process. Consistent with this assumption, neutrophil depletion promoted wound healing in normal and in particular in diabetic mice [21]. Furthermore, high abundance and long persistence of neutrophils are a hallmark of chronic human wounds, resulting in oxidative stress and tissue damage [48–50].

Macrophages also showed an early peak in healthy mice, which was delayed, but then more intense in diabetic mice. Interestingly, depletion of monocytes/macrophages early after wounding severely impaired the healing process in healthy mice [27], suggesting that the reduced numbers of these cells in early wounds of diabetic versus control mice contributes to the impaired healing. By contrast, they were more abundant in late wounds of db/db versus healthy mice, which may cause prolonged tissue damage due to high ROS production. Consistent with this assumption, a prolonged presence of inflammatory macrophages as seen in chronic skin ulcers caused impaired healing through promotion of inflammation and induction of fibroblast senescence [51]. In the future, it will be important to further characterize the macrophage phenotype in normal and diabetic mice and at different stages of the healing process.

Surprisingly, there is as yet little knowledge on the role of LCs in the repair process. These cells may have a beneficial function, since their repopulation after wounding correlated with better healing of diabetic foot ulcers [30]. LCs activate the adaptive arm of the immune system and are important regulators of skin homeostasis [52]. Consistent with published data on the early kinetics of LCs during wound healing in human skin/SCID mouse models [12], the absolute numbers of $MHCII^+$ LCs even increased post wounding and remained high until day 15. The accumulation of LCs at the wound edge that we observed by immunostaining suggests that LCs proliferate in the wound epidermis and/or the immediate surrounding. We also observed that diabetic mice have less LCs compared to healthy mice throughout the course of wound healing, which may well contribute to their impaired healing. In the future, it will be important to study the functional relevance of LCs for wound healing by depletion of these cells.

We observed different kinetics of cDC1 and cDC2 during the healing process, indicating different functions of the DC subtypes during wound healing. The abundance of both cDC1 and cDC2 in the late granulation tissue suggests roles in tissue remodeling, which remain to be determined.

Finally, we found a strong reduction in the number and frequencies of eosinophils in unwounded and wounded skin of diabetic versus healthy mice. This may be functionally important, since eosinophils were shown to produce transforming growth factor (TGF)-α and TGF-β during wound healing in hamsters [53]. A histochemical study showed early infiltration of eosinophils into rabbit wounds, followed by a decline [54] as also seen in our flow cytometry study. Surprisingly, however, their depletion using neutralizing IL-5 antibodies promoted the closure of excisional wounds in hamsters as shown by macroscopic analysis of the wounds [55]. Future eosinophil depletion studies followed by histological and molecular assessment of the wounds will be required to further assess the specific roles of these cells in the repair process.

Taken together, the results obtained in this study point to functions of so far poorly characterized myeloid subtypes at different stages of the healing process and show their dysregulation in diabetic mice. Therefore, these data will be important for the design of strategies to deplete/target them during different stages of wound healing and to unravel their roles in the normal repair process and in the pathogenesis of wound healing disorders.

Materials and methods

Wounding of mice

Female WT C57BL/6 mice and genetically diabetic C57BLKSJ-lepr $^{db/db}$ mice (8–9 weeks of age; Elevage Janvier, Le Genest-Saint-Isle, France) were anaesthetized, and four full-thickness excisional wounds of 5 mm diameter were generated on their back using disposable biopsy punches [56]. Wounds were allowed to heal without dressing and harvested after euthanasia of the mice. The back skin wounds and unwounded skin were excised with a 5 mm biopsy punch, placed in a 1.5-mL tube with RPMI medium supplemented with L-glutamine and HEPES (RPMI 1640, HEPES; Gibco, Thermo Fisher Scientific, Waltham, MA) and kept on ice until further processing. All experiments with mice had been approved by the local veterinary authorities (Kantonales Veterinäramt Zürich, permission given to S.W.).

Immunohistochemistry staining of wound sections

Wounds were excised, bisected, and directly frozen in tissue freezing medium (Leica Biosystems, Wetzlar, Germany) without prior fixation. Frozen sections (7 μm) were fixed for 10 min with 4% paraformaldehyde and analyzed by immunohistochemistry staining [39] using rat-anti-langerin/CD207 IgG2a (eBioL31, Thermo Fisher), the Vectastain ABC peroxidase kit, and the diaminobenzidine peroxidase substrate kit (both from Vector Laboratories, Burlingame, CA).

Dissociation of wound and skin tissue and flow-cytometric analysis

Skin and wound samples were intensely cut into small pieces using surgical scissors. For C57BL/6 mice, the resulting mash was

transferred to 15-mL conical tubes containing Mg^{2+}/Ca^{2+}-free 1× PBS before adding EGTA (10 mM final concentration) and incubation at 37°C under continuous shaking (65 rpm) for 20 min. The tissue mash was pelleted by centrifugation and washed twice with 1× PBS. Samples were resuspended in 2–4 mL RPMI 1640/HEPES medium and predigested using Liberase TL (1.3 WU/mL final; Roche, Rotkreuz, Switzerland) treatment at 37°C and shaking at 65 rpm for 60 min. The mashed skin and wound samples from C57BLKSJ-lepr $^{db/db}$ mice were directly resuspended in 2–4 mL RPMI 1640/HEPES medium and predigested as described for non-diabetic mice.

The predigested tissue was loosened by vigorous manual shaking, and medium containing Dispase II (1 KU/mL final; Gibco, Paisley, UK), bovine DNase I (0.2 mg/mL final; Sigma, Munich, Germany), and $MgCl_2$ (7.5 mM final concentration) was added. Samples were incubated at 37°C under continuous shaking at 80 rpm for 15 min, followed by incubation at room temperature and shaking at 80 rpm for additional 15 min. The cell suspension was diluted with 1× PBS and passed through a 30 μm cell strainer (CellTrics; Sysmex, Horgen, Switzerland). Cells were pelleted by centrifugation, transferred to a 96-well V-bottom plate (Sarstedt, Nürnbrecht, Germany), and labeled for flow cytometry analysis [57].

Cells were processed in 96-well V-bottom plates, and all staining/fixation steps were performed at 4°C in the dark. They were washed with 1× PBS and stained for 30 min in 1× PBS containing a dye that selectively stains viable cells and antibodies directed against different cell surface markers. To minimize nonspecific binding, Fc receptor block (anti-mouse CD16/CD32, BioLegend, San Diego, CA) was included. Following cell surface staining, cells were washed with flow buffer (1× PBS, 2% FBS, 5 mM EGTA), fixed for 1 h (Cytofix/Cytoperm; BD Biosciences, Franklin Lakes, NJ) and washed once with 1× permeabilization buffer. For intracellular staining, antibodies were diluted in 1× permeabilization buffer and cells were stained overnight. They were then washed with permeabilization buffer, resuspended in flow buffer, and stored at 4°C in the dark until acquisition.

Cell acquisition and analysis was performed with the help of the ETH Flow Cytometry core facility, which defines high-quality flow cytometry guidelines. Stained cells were analyzed using a BD LSRII Fortessa (BD Biosciences) equipped with FACS-Diva software (Version 6; BD Biosciences). Compensation of fluorescence emission was performed using compensation beads (BD Biosciences). Samples were acquired using Fortessa's HTS plate reader option at an event rate of around 10 000 ev/s. Staining and gating controls included fluorescence minus one samples.

Compensation adjustment, gating, and data analysis were performed using FlowJo software (Version X, Tree Star Inc., Ashland, OR), and data were exported for further processing.

The dyes and antibodies used for flow cytometry are listed below.

Dyes and antibodies for flow cytometry

Antigen	Clone	Fluorophore	Dilution	Source
CD16/32	93	None	1:200	BD Biosciences
CD45	30-F11	AF- 700	1:1000	BioLegend
CD11b	M1/70	BV 605	1:2000	BioLegend
XCR1	ZET	PerCP-Cy5.5	1:300	BD Biosciences
CD172a	P84	FITC	1:100	BioLegend
(or)CD172a	P84	Biotin	1:100	eBioscience,
Secondary		BV 711	1:1000	Vienna, Austria BD Biosciences
CD24	M1/69	BV 421	1:1000	BioLegend
CD11c	N418	PE-Cy7	1:1000	BioLegend
F4/80	BM8	BV 785	1:200	BioLegend
Ly6C	HK1.4	APC-Cy7	1:800	BioLegend
I-A/I-E	M5/ 114.15.2	BV 650	1:3000	BioLegend
CD64	X54-5/7.1	APC	1:200	BioLegend
Ly6G	1A8	Biotin	1:200	BioLegend
Secondary	1A8	BV 711	1:1000	BD Biosciences
Or		FITC	1:200	BioLegend
Ly6G				
Live/Dead		Zombie Aqua	1:400	BioLegend
CD3	145-2C11	PE	1:300	eBioscience
CD19	1D3	PE	1:500	eBioscience
NK 1.1	PK136	PE	1:300	eBioscience
CD207	eBioL31	Biotin	1:200	eBioscience
Secondary		BV 711	1:1000	BD Biosciences
Siglec-F	E50-2440	PE	1:300	BD Biosciences

Dimensionality reduction and clustering

Flow cytometry data were preprocessed using FlowJo software to select the population of interest in each sample. These populations, which were characterized as live, singlets, $CD45^+$ cells, were subsampled (3000 cells per sample in C57BL/6 mice and 1500 per sample in db/db mice) and concatenated to one file per experiment.

These .fcs files were then used for the generation of t-SNE maps and identification of cell clusters with PhenoGraph [58]. PhenoGraph was designed to ease the analysis of high-dimensional single-cell data. It creates a network representing similarities (defined by the measured markers) between cells and then identifies clusters. These clusters are based on the k-nearest neighbor algorithm. Heatmaps and dendrograms were created using R and the packages stats, qplot, and flowCore (Bioconductor, Seattle, WA).

Robust locally weighted regression (Loess)

Loess regression is a commonly used nonparametric, local regression. The weight of data points is estimated iteratively using robust estimation techniques [44]. For the smoothing parameter α, the default of 0.75 was used. Loess was applied on manually retrieved cell numbers and frequencies using R [59]. The graphs were created using ggplot2 [60].

Acknowledgements: We thank Rin Okumura, ETH Zurich, for excellent technical assistance. This work was supported by the Swiss National Science Foundation (grants 31003A_169204 to S.W and 310030B_182829 to M.K.), the ETH Zurich (to M.K and S.W.), and by University Medicine Zurich (flagship project SKINTEGRITY to S.W.).

Conflict of interest: The authors declare no financial or commercial conflict of interest.

References

1 **Gurtner, G. C., Werner, S., Barrandon, Y. and Longaker, M. T.**, Wound repair and regeneration. *Nature* 2008. **453**: 314–321.

2 **Eming, S. A., Martin, P. and Tomic-Canic, M.**, Wound repair and regeneration: mechanisms, signaling, and translation. *Sci. Transl. Med.* 2014.**6**: 265–266.

3 **Haertel, E., Werner, S. and Schafer, M.**, Transcriptional regulation of wound inflammation. *Semin. Immunol.* 2014. **26**: 321–328.

4 **Antsiferova, M., Martin, C., Huber, M., Feyerabend, T. B., Forster, A., Hartmann, K., Rodewald, H. R. et al.**, Mast cells are dispensable for normal and activin-promoted wound healing and skin carcinogenesis. *J. Immunol.* 2013. **191**: 6147–6155.

5 **Greenhalgh, D. G., Sprugel, K. H., Murray, M. J. and Ross, R.**, PDGF and FGF stimulate wound healing in the genetically diabetic mouse. *Am. J. Pathol.* 1990. **136**: 1235–1246.

6 **Tsuboi, R. and Rifkin, D. B.**, Recombinant basic fibroblast growth factor stimulates wound healing in healing-impaired db/db mice. *J. Exp. Med.* 1990. **172**: 245–251.

7 **Gao, M., Nguyen, T. T., Suckow, M. A., Wolter, W. R., Gooyit, M., Mobashery, S. and Chang, M.**, Acceleration of diabetic wound healing using a novel protease-anti-protease combination therapy. *Proc. Natl. Acad. Sci. U S A.* 2015. **112**: 15226–15231.

8 **Das, A., Ghatak, S., Sinha, M., Chaffee, S., Ahmed, N. S., Parinandi, N. L., Wohleb, E. S. et al.**, Correction of MFG-E8 resolves inflammation and promotes cutaneous wound healing in diabetes. *J. Immunol.* 2016. **196**: 5089–5100.

9 **Bannon, P., Wood, S., Restivo, T., Campbell, L., Hardman, M. J. and Mace, K. A.**, Diabetes induces stable intrinsic changes to myeloid cells that contribute to chronic inflammation during wound healing in mice. *Dis. Model. Mech.* 2013. **6**: 1434–1447.

10 **Wicks, K., Torbica, T. and Mace, K. A.**, Myeloid cell dysfunction and the pathogenesis of the diabetic chronic wound. *Semin. Immunol.* 2014. **26**: 341–353.

11 **Tamoutounour, S., Guilliams, M., Montanana Sanchis, F., Liu, H., Terhorst, D., Malosse, C., Pollet, E. et al.**, Origins and functional specialization of macrophages and of conventional and monocyte-derived dendritic cells in mouse skin. *Immunity* 2013. **39**: 925–938.

12 **Juhasz, I., Simon, M., Jr., Herlyn, M. and Hunyadi, J.**, Repopulation of Langerhans cells during wound healing in an experimental human skin/SCID mouse model. *Immunol Lett.* 1996. **52**: 125–128.

13 **Martin, P. and Leibovich, S. J.**, Inflammatory cells during wound repair: the good, the bad and the ugly. *Trends. Cell Biol.* 2005. **15**: 599–607.

14 **Agaiby, A. D. and Dyson, M.**, Immuno-inflammatory cell dynamics during cutaneous wound healing. *J. Anat.* 1999.**195** (Pt 4): 531–542.

15 **Kim, M. H., Liu, W., Borjesson, D. L., Curry, F. R., Miller, L. S., Cheung, A. L., Liu, F. T., Isseroff, R. R. and Simon, S. I.**, Dynamics of neutrophil infiltration during cutaneous wound healing and infection using fluorescence imaging. *J. Invest. Dermatol.* 2008. **128**: 1812–1820.

16 **Crane, M. J., Daley, J. M., van Houtte, O., Brancato, S. K., Henry, W. L., Jr. and Albina, J. E.**, The monocyte to macrophage transition in the murine sterile wound. *PLoS One* 2014. **9**: e86660.

17 **Kolaczkowska, E. and Kubes, P.**, Neutrophil recruitment and function in health and inflammation. *Nat. Rev. Immunol.* 2013. **13**: 159–175.

18 **Borregaard, N.**, Neutrophils, from marrow to microbes. *Immunity* 2010. **33**: 657–670.

19 **Theilgaard-Monch, K., Knudsen, S., Follin, P. and Borregaard, N.**, The transcriptional activation program of human neutrophils in skin lesions supports their important role in wound healing. *J. Immunol.* 2004. **172**: 7684–7693.

20 **Simpson, D. M. and Ross, R.**, The neutrophilic leukocyte in wound repair a study with antineutrophil serum. *J. Clin. Invest.* 1972. **51**: 2009–2023.

21 **Dovi, J. V., He, L. K. and DiPietro, L. A.**, Accelerated wound closure in neutrophil-depleted mice. *J. Leukoc. Biol.* 2003. **73**: 448–455.

22 **Wong, S. L., Demers, M., Martinod, K., Gallant, M., Wang, Y., Goldfine, A. B., Kahn, C. R. and Wagner, D. D.**, Diabetes primes neutrophils to undergo NETosis, which impairs wound healing. *Nat. Med.* 2015. **21**: 815–819.

23 **Fadini, G. P., Menegazzo, L., Rigato, M., Scattolini, V., Poncina, N., Bruttocao, A., Ciciliot, S. et al.**, NETosis delays diabetic wound healing in mice and humans. *Diabetes* 2016. **65**: 1061–1071.

24 **Martin, P., D'Souza, D., Martin, J., Grose, R., Cooper, L., Maki, R. and McKercher, S. R.**, Wound healing in the PU.1 null mouse–tissue repair is not dependent on inflammatory cells. *Curr. Biol.* 2003. **13**: 1122–1128.

25 **Leibovich, S. J. and Ross, R.**, The role of the macrophage in wound repair. A study with hydrocortisone and antimacrophage serum. *Am. J. Pathol.* 1975. **78**: 71–100.

26 **Willenborg, S., Lucas, T., van Loo, G., Knipper, J. A., Krieg, T., Haase, I., Brachvogel, B. et al.**, CCR2 recruits an inflammatory macrophage subpopulation critical for angiogenesis in tissue repair. *Blood* 2012. **120**: 613–625.

27 **Lucas, T., Waisman, A., Ranjan, R., Roes, J., Krieg, T., Muller, W., Roers, A. and Eming, S. A.**, Differential roles of macrophages in diverse phases of skin repair. *J. Immunol.* 2010. **184**: 3964–3977.

28 **Goren, I., Allmann, N., Yogev, N., Schurmann, C., Linke, A., Holdener, M., Waisman, A. et al.**, A transgenic mouse model of inducible macrophage depletion: effects of diphtheria toxin-driven lysozyme M-specific cell lineage ablation on wound inflammatory, angiogenic, and contractive processes. *Am. J. Pathol.* 2009. **175**: 132–147.

29 **Low, Q. E., Drugea, I. A., Duffner, L. A., Quinn, D. G., Cook, D. N., Rollins, B. J., Kovacs, E. J. and DiPietro, L. A.**, Wound healing in MIP-1alpha(-/-) and MCP-1(-/-) mice. *Am. J. Pathol.* 2001. **159**: 457–463.

30 **Stojadinovic, O., Yin, N., Lehmann, J., Pastar, I., Kirsner, R. S. and Tomic-Canic, M.**, Increased number of Langerhans cells in the epidermis of diabetic foot ulcers correlates with healing outcome. *Immunol. Res.* 2013. **57**: 222–228.

31 **Gregorio, J., Meller, S., Conrad, C., Di Nardo, A., Homey, B., Lauerma, A., Arai, N. et al.**, Plasmacytoid dendritic cells sense skin injury and promote wound healing through type I interferons. *J. Exp. Med.* 2010. **207**: 2921–2930.

32 **Haertel, E., Joshi, N., Hiebert, P., Kopf, M. and Werner, S.**, Regulatory T cells are required for normal and activin-promoted wound repair in mice. *Eur. J. Immunol.* 2018. **48**: 1001–1013.

33 **Guilliams, M., Dutertre, C. A., Scott, C. L., McGovern, N., Sichien, D., Chakarov, S., Van Gassen, S. et al.**, Unsupervised high-dimensional analysis aligns dendritic cells across tissues and species. *Immunity* 2016. **45**: 669–684.

34 **Poulin, L. F., Henri, S., de Bovis, B., Devilard, E., Kissenpfennig, A. and Malissen, B.**, The dermis contains langerin+ dendritic cells that develop and function independently of epidermal Langerhans cells. *J. Exp. Med.* 2007. **204**: 3119–3131.

35 **Miloud, T., Hämmerling, G. J. and Garbi, N.**, Review of murine dendritic cells: types, location and development. *Methods Mol. Biol.* 2010. **595**: 21–41.

36 **Malissen, B., Tamoutounour, S. and Henri, S.**, The origins and functions of dendritic cells and macrophages in the skin. *Nat. Rev. Immunol.* 2014. **14**: 417–428.

37 **Ng, M. F.**, The role of mast cells in wound healing. *Int. Wound. J.* 2010. **7**: 55–61.

38 **Willenborg, S., Eckes, B., Brinckmann, J., Krieg, T., Waisman, A., Hartmann, K., Roers, A. and Eming, S. A.**, Genetic ablation of mast cells redefines the role of mast cells in skin wound healing and bleomycin-induced fibrosis. *J. Invest. Dermatol.* 2014. **134**: 2005–2015.

39 **Hiebert, P., Wietecha, M. S., Cangkrama, M., Haertel, E., Mavrogonatou, E., Stumpe, M., Steenbock, H. et al.**, Nrf2-mediated fibroblast reprogramming drives cellular senescence by targeting the matrisome. *Dev. Cell* 2018.**46**: 145–161.e110.

40 **Neefjes, J., Jongsma, M. L., Paul, P. and Bakke, O.**, Towards a systems understanding of MHC class I and MHC class II antigen presentation. *Nat. Rev. Immunol.* 2011. **11**: 823–836.

41 **Schaffer, M., Bongartz, M., Hoffmann, W. and Viebahn, R.**, MHC-class-II-deficiency impairs wound healing. *J. Surg. Res.* 2007. **138**: 100–105.

42 **Mair, F., Hartmann, F. J., Mrdjen, D., Tosevski, V., Krieg, C. and Becher, B.**, The end of gating? An introduction to automated analysis of high dimensional cytometry data. *Eur. J. Immunol.* 2016. **46**: 34–43.

43 **Becher, B., Schlitzer, A., Chen, J., Mair, F., Sumatoh, H. R., Teng, K. W., Low, D. et al.**, High-dimensional analysis of the murine myeloid cell system. *Nat. Immunol.* 2014. **15**: 1181–1189.

44 **Cleveland, W. S.**, Robust locally weighted regression and smoothing scatterplots. *J. Am. Statist. Assoc.* 1979. **74**: 829–836.

45 **Efron, B. and Tibshirani, R.**, Statistical data analysis in the computer age. *Science* 1991. **253**: 390–395.

46 **Eming, S. A., Krieg, T. and Davidson, J. M.**, Inflammation in wound repair: molecular and cellular mechanisms. *J. Invest. Dermatol.* 2007. **127**: 514–525.

47 **Wilgus, T. A., Roy, S. and McDaniel, J. C.**, Neutrophils and wound repair: positive actions and negative reactions. *Adv. Wound Care (New Rochelle)* 2013. **2**: 379–388.

48 **Diegelmann, R. F.**, Excessive neutrophils characterize chronic pressure ulcers. *Wound Repair Regen* 2003. **11**: 490–495.

49 **Wlaschek, M. and Scharffetter-Kochanek, K.**, Oxidative stress in chronic venous leg ulcers. *Wound Repair Regen* 2005. **13**: 452–461.

50 **McDaniel, J. C., Roy, S. and Wilgus, T. A.**, Neutrophil activity in chronic venous leg ulcers—a target for therapy? *Wound Repair Regen* 2013. **21**: 339–351.

51 **Sindrilaru, A., Peters, T., Wieschalka, S., Baican, C., Baican, A., Peter, H., Hainzl, A. et al.**, An unrestrained proinflammatory M1 macrophage population induced by iron impairs wound healing in humans and mice. *J. Clin. Invest.* 2011. **121**: 985–997.

52 **Seneschal, J., Clark, R. A., Gehad, A., Baecher-Allan, C. M. and Kupper, T. S.**, Human epidermal Langerhans cells maintain immune homeostasis in skin by activating skin resident regulatory T cells. *Immunity* 2012. **36**: 873–884.

53 **Wong, D. T., Donoff, R. B., Yang, J., Song, B. Z., Matossian, K., Nagura, N., Elovic, A. et al.**, Sequential expression of transforming growth factors alpha and beta 1 by eosinophils during cutaneous wound healing in the hamster. *Am. J. Pathol.* 1993. **143**: 130–142.

54 **Song, B. Z., Donoff, R. B., Tsuji, T., Todd, R., Gallagher, G. T. and Wong, D. T.**, Identification of rabbit eosinophils and heterophils in cutaneous healing wounds. *Histochem. J.* 1993. **25**: 762–771.

55 **Yang, J., Tyler, L. W., Donoff, R. B., Song, B., Torio, A. J., Gallagher, G. T., Tsuji, T. et al.**, Salivary EGF regulates eosinophil-derived TGF-alpha expression in hamster oral wounds. *Am. J. Physiol.* 1996. **270**: G191–G202.

56 **Joshi, N. and Werner, S.**, Nrf2 is highly expressed in neutrophils, but myeloid cell-derived Nrf2 is dispensable for wound healing in mice. *PLoS One* 2017. **12**: e0187162.

57 **Sand, J., Haertel, E., Biedermann, T., Contassot, E., Reichmann, E., French, L. E., Werner, S. and Beer, H. D.**, Expression of inflammasome proteins and inflammasome activation occurs in human, but not in murine keratinocytes. *Cell. Death. Dis.* 2018. **9**: 24.

58 **Levine, J. H., Simonds, E. F., Bendall, S. C., Davis, K. L., Amir el, A. D., Tadmor, M. D., Litvin, O. et al.**, Data-driven phenotypic dissection of AML reveals progenitor-like cells that correlate with prognosis. *Cell* 2015. **162**: 184–197.

59 R Core Team: A Language and Environment for Statistical Computing. *Foundation for statistical computing*. Vienna, Austria, 2013. http://www.R-project.org

60 **Wickham, H.**, *Elegant graphics for data analysis*, Springer Verlag, New York, 2016.

Abbreviations: **cDC**: conventional DC · **LC**: Langerhans cell · **t-SNE**: t-Distributed Stochastic Neighbor Embedding

Full correspondence: Prof. Sabine Werner, Institute of Molecular Health Sciences, Otto-Stern-Weg 7, 8093 Zurich, Switzerland
e-mail: sabine.werner@biol.ethz.ch

Additional correspondence: Prof. Manfred Kopf, Institute of Molecular Health Sciences, Otto-Stern-Weg 7, 8093 Zurich, Switzerland
e-mail: manfred.kopf@biol.ethz.ch

The peer review history for this article is available at https://publons.com/publon/10.1002/eji.201948438

Received: 16/10/2019
Revised: 18/2/2020
Accepted: 16/4/2020
Accepted article online: 19/4/2020